Engineered Science

REVIEW PAPER

View Article Online

Nitrogen Coordinated Single Atomic Metals Supported on Nanocarbons: A New Frontier in Electrocatalytic CO_2 Reduction

Fuping Pan, Xianmei Xiang and Ying Li*

The rising level of atmospheric CO_2 caused by increased fossil energy consumption is linked to global warming effects. Electrochemical CO_2 reduction (CO_2RR) can convert CO_2 into value-added chemical fuels by using renewable energy-generated electricity as the energy input, providing a promising solution to mitigate the CO_2 emissions. Compared to conventional precious metal catalysts for CO_2RR, carbon-based catalysts are made of earth-abundant elements and less expensive, with great potential for large-scale applications. In this Review, recent advances of designing and synthesizing nitrogen coordinated single atomic transition metals supported on nanocarbons ($M{-}N_X$-C; M=Fe, Ni, Co) as electrocatalysts for CO_2RR are reviewed from both experimental and computational aspects. The catalytic mechanisms and design principles are highlighted, and the correlations of catalyst synthesis-structure-performance relationships are discussed. The disparities in catalytic activity between noble metal catalysts (Ag and Au) and $M{-}N_X$-C catalysts suggest that there is still much room to develop more advanced $M{-}N_X$-C catalysts. Therefore, several strategies, including mechanism exploration, $M{-}N_X$ sites and carbon supports engineering, and large-scale fabrication of atomically dispersed catalysts and reactor systems design are proposed to propel the use of $M{-}N_X$-C for achieving high-efficient and cost-effective CO_2-to-fuels conversion.

Keywords: Atomic catalysts; metal-nitrogen coordination; nanocarbons; CO_2 reduction; electrocatalysis

Received 20th March 2018, Accepted 24th April 2018

DOI: 10.30919/es.1804232

1. Background and motivation

The heavy dependency on fossil fuels for the production of energy and the increasing human activities lead to the massive emissions of greenhouse gases, mainly CO_2, into the atmosphere. The atmospheric concentration of CO_2 has rapidly increased from 322 ppm in 1967 to 407 ppm in 2017, which is estimated to reach 600 ppm by 2100.[1] The ever-increasing CO_2 emissions have disastrous consequences on global warming, climate change, human's health, and extinction of species. The ideal approach to mitigate these changes caused by CO_2 emissions is to convert CO_2 into harmless or useful products, which requires the development of green and sustainable strategies for efficient and massive CO_2 conversion.

Various CO_2 conversion approaches have been developed and pursued intensively, including thermochemical reforming,[2–4] biochemical conversion,[5,6] photocatalysis,[7–10] and electrocatalytic reduction.[11–14] Among these techniques, the electrocatalytic CO_2 reduction in aqueous media is believed to be a more promising route because of the following advantages: easy manipulation at ambient conditions, low-cost process only using abundant water and CO_2 as feedstock, and high viability of large-scale applications.[12,15,16] More attractively, the CO_2 electrolysis process can be powered by clean electricity generated from solar, wind, geothermal, and tidal energy, and thus this technology can not only mitigate atmospheric CO_2 concentrations but also store intermittent renewable energy in the form of transportable fuels simultaneously. In this case, the carbon-neutral society could be achieved, which will be beneficial to the sustainable development.[17]

However, this desired CO_2-to-electrofuels solution imposes great technological challenges because CO_2 is a fully oxidized and thermodynamically stable molecule because of its linear and centrosymmetric molecular structure, which makes CO_2 reduction reaction (CO_2RR) very difficult to occur and requires large overpotentials.[14,18,19] Combined with challenges of possible multiple products and competition over hydrogen evolution reaction (HER), a suitable catalyst is thus essential to achieve a sustainable CO_2 reduction process with high efficiency, selectivity, and stability. Through screening catalysts with different topography, compositions, and structures by experimental and theoretical routes, to date, a variety of electrocatalysts have been designed and fabricated, including noble metals,[20–22] transition metal oxides/chalcogenides,[12,23,24] metal-free carbons,[1,25] and single atomic nitrogen coordinated metals supported on carbons ($M{-}N_X$-C).[26–29] Up to now, there have been several excellent reviews that systematically summarized and commented the advancements and progresses achieved on these heterogonous catalysts except $M{-}N_X$-C because $M{-}N_X$-C was very recently discovered for CO_2 reduction.[1,12,30] Taking advantages of low-cost carbon as supports,[31–33] maximum atom efficiency of isolated M,[27,34] and optimal binding strength between $M{-}N_X$ and CO intermediate,[35] high-efficient and selective reduction of CO_2 to CO has been demonstrated on $M{-}N_X$-C,[26,27,36] making $M{-}N_X$-C promising

---

Department of Mechanical Engineering, Texas A&M University, College Station, Texas 77843, USA. E-mail: yingli@tamu.edu

electrocatalysts for future large-scale CO_2 electrolysis. Therefore, it is important and necessary to summarize and discuss the current achievements in the design, preparation, catalytic activity and mechanism of M−N_X-C for CO_2 reduction, which will provide insights on the fabrication of next-generation M−N_X-C catalysts for realizing an efficient and cost-effective electrochemical CO_2-to-fuels process.

In this review, we present the recent progresses of CO_2RR on single-atomic M−N_X-C and perspectives on the rational design of advanced catalysts. We first start with an introduction of the fundamental theory regarding atomic configurations, catalytic mechanisms, and design principles of M−N_X-C for CO_2RR. We then discuss three types of M−N_X-C classified by metal centers including Fe, Ni, and Co, and correlate their structure and compositions with activity and selectivity to unveil the underlying catalytic role of various metal centers. Finally, the challenges and opportunities on the design of advanced M−N_X-C in this emerging area are discussed.

2. Identification of the atomic structure of M−N_X sites

The M−N_X sites are comprised of the electronic coordination between M centers and N atoms inserted into carbon lattices.[37] As for N structures, it has been widely accepted that N doping can occur either via substituting carbon atoms in the graphitic structure or reacting between gaseous N-based sources with oxygen-containing functionalities of carbons, which commonly leads to the formation of edge-like pyridinic N, five-membered heterocyclic rings-like pyrollic N, and bulk-like graphitic N.[38−43] Among them, it was demonstrated that metals ions preferentially coordinate with pyridinic N rather than graphitic N due to the existence of lone-pair electron on pyridinic N.[26,44] When a chemical bond between M and N is formed, the binding energy of pyridinic N shifts to a higher value owing to the introduction of an ion withdrawing effect caused by the replacement of a proton on pyridinic N by a metal ion. This change in the electronic environment of N atoms has been experimentally confirmed by X-ray photoelectron spectroscopy (XPS) analyses.[26,45,46]

It has been demonstrated that M−N_X complexes can be formed by the electronic interaction between M and N atoms during the annealing of M,N,C-containing precursors at high temperatures.[47−49] However, since the single M atoms tend to aggregate during the high-temperature process due to their high mobility, the metallic phases can be commonly generated simultaneously.[50−53] Thus, the accurate recognition of single-atomic M−N_X is relatively difficult caused by the co-presence of multiple heterogeneous components, which commonly requires the use of advanced electron microscopy and spectroscopy to distinguish the M−N coordination from metallic clusters and particles. High-angle angular dark-field scanning transmission electron microscopy (HAADF-STEM) is a powerful technique to image isolated M atoms. By using HAADF-STEM, Chung et al.[54] realized the direct identification of the atomic structure of Fe−N_X. The STEM image in Figure 1a shows single atoms dispersed across the carbon surface with dots exhibiting bright contrast, which were confirmed to be primarily Fe by electron energy loss spectroscopy (EELS) (Figure 1b). However, the EELS spectrum was recorded from a very limited area of ~1 to 2 Å combined with the instability of the individual Fe atom, and the weak signal makes it impossible to determine the valence states of the individual Fe from EEL fine-structure analysis.

To further identify the chemical state of M centers and their local coordination with N, X-ray absorption spectroscopy (XAS) is commonly performed using synchrotron radiation sources, including extended X-ray absorption fine structure (EXAFS) and X-ray absorption near edge structure (XANES).[27,55,57] These methods are very powerful for discriminating M−N, M−C, and M−M bonds. Fei et al.[55] conducted thorough analyses of various M−N_X moieties (M=Fe, Co, Ni) by comparing experimental and simulated EXAFS spectra on M−N_X-C catalysts. From their results (Figure 1c), the single M centers with four N atoms and one adsorbed O atom in the first coordination sphere and four C atoms in the second coordination sphere were confirmed. This directly reveals the formation of M−N_4 moiety, where the M is bonded with four N atoms embedded in the carbon lattices. On the other hand, Mossbauer spectroscopy has also been used to discriminate the geometric structure of Fe−N_X. Recent findings manifested that two kinds of Fe−N_4 could be generally formed in Fe−N_4-C synthesized by thermal treatment of Fe, N, and C-containing precursors.[58,59] One is the bulk-hosted Fe−N_4 moieties (Figure 1d), which embeds in the bulk of a graphitic layer and is fully encapsulated by carbon atoms. Another is the edge-hosted Fe−N_{2+2} (Figure 1e), where two N-doped graphitic layers are connected by a Fe atom bonded with two N atoms at the edges of each graphitic layer. The formation of Fe−N_{2+2} also leads to a distortion of carbon plane environment that causes the out-of-plane position of Fe, while the Fe−N_4 maintains the in-plane structure.[58,59] In addition, many kinds of Fe−N_X (x=2, 5, 6)[60−62] and Co−N_X (x= 2, 3, 4)[36,48] structures have also been proposed as possible configurations in M−N_X-C. Although these advancements on identifying the structure of M−N_X have been achieved, there is still a debate for the structural configurations of M−N_X because various synthetic routes and parameters will give a broad possibility on the formation of different M−N_X moieties. Future works are suggested to combine above-mentioned characterization techniques together to determine the detailed structure of M−N_X in a specific catalyst.

3. Fundamentals of CO_2RR on M−N_X-C

3.1. Mechanism

Electrochemical CO_2 reduction is commonly conducted in a two-chamber electrolyzer consisting of an anode and a cathode separated with an ion conducting membrane to protect the re-oxidization of reduced products. At the anode, water is oxidized to oxygen and produce proton (H^+), whereas CO_2 is reduced to carbon-containing pieces at the cathode. The overall process involves the formation of H^+ at the anode, migration of H^+ through the electrolyte, and reaction of H^+ with CO_2 at the catalytic sites of the cathode to form products.[12] For CO_2RR on M−N_X-C, three major steps are commonly involved: i) chemical adsorption of CO_2 on M sites; ii) CO_2 activation, electron transfer and combination with H^+ to cleave C−O bonds and/or form C−H bonds; and iii) configuration rearrangement of intermediates and products desorption from M−N_X-C surface to electrolyte.[12,56] The molecular-level insight into the activation and reduction of CO_2 on Ni−N_4 under *operando* conditions has been investigated by Yang et al.[27] It was found that the delocalization of the unpaired electron in the $3d_{x2-y2}$ orbital and spontaneous charge transfer from monovalent Ni(I) to

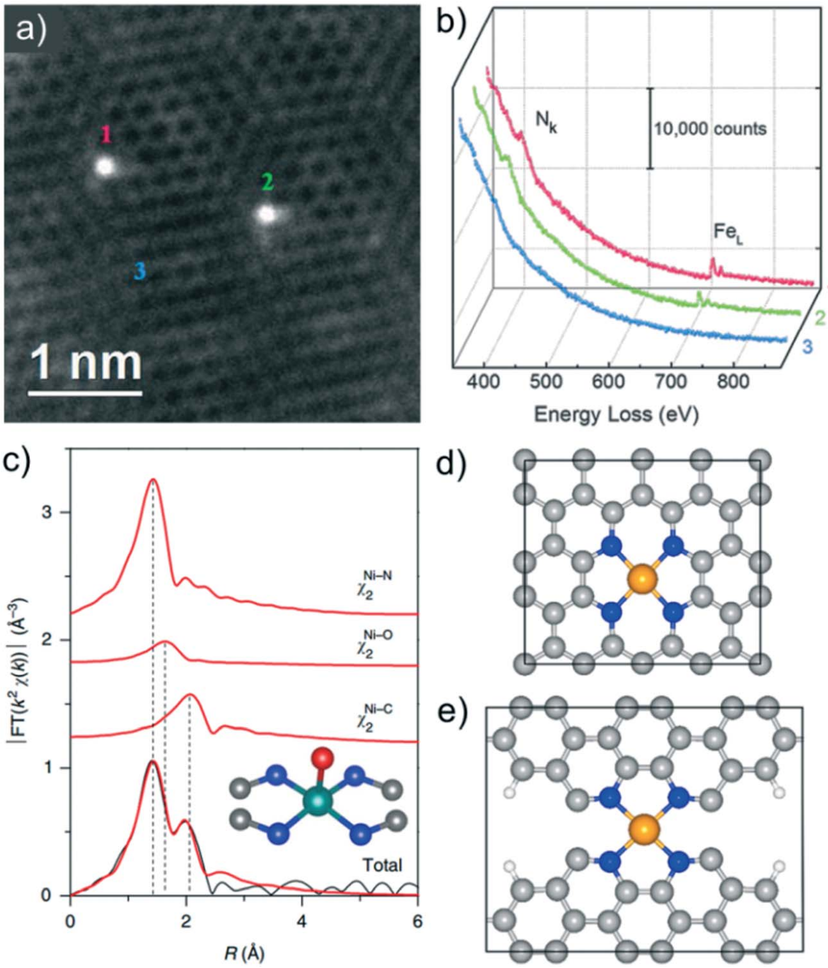

Fig. 1 (a) HAADF-STEM image of individual Fe atoms (labeled 1, 2, and 3) in a few-layer graphene sheet. (b) EEL spectra of the N K-edge (N_K) and Fe L-edge (Fe_L) acquired from single atoms (1 and 2) and few-layer graphene (3), demonstrating the presence of N around the Fe atoms. Reproduced with permission from ref. 54 Copyright 2017, Science. (c) Ni K-edge EXAFS analysis of an atomic M−N_4-C in R spaces. Curves from top to bottom are the Ni−N, Ni−O and Ni−C two-body backscattering signals χ^2 included in the fit and the total signal (red line) superimposed on the experimental signal (black line). The measured and calculated spectra show excellent agreement. The inset in d shows the structure of a Ni−N_4 moiety derived from the EXAFS result, where the teal, red, blue and grey spheres represent Ni, O, N and C, respectively. Reproduced with permission from ref. 55 Copyright 2018, Nature. The proposed structures of bulk-hosted M−N_4 (d) and edge-hosted M−N_{2+2} (e). Reproduced with permission from ref. 56 Copyright 2018, ACS. In the figure, the gray, blue, yellow, red, and white balls represent C, N, M, O, and H atoms, respectively.

the carbon *2p* orbital in CO_2 to form a $CO_2^{\delta-}$ species took place after adsorbing CO_2 on Ni−N_4 via bonding between Ni atoms of Ni−N_4 and C atom of CO_2. DFT calculations further indicated that the increase in the density of states around 3−6 eV below the Fermi level results from the 1π orbital of the bent CO_2 molecules adsorbed on Ni(i) and the delocalization of the Ni 3d orbital. During electrochemical CO_2 reduction, the recovery of low-oxidation-state Ni after one cycle of CO_2 reduction took place, in which the CO was produced through ($Ni(I)^* + CO_2 + 2H^+ + 2e^- \rightarrow Ni(I)^* + CO + H_2O$), as shown in Figure 2.

3.2. Selectivity

Since CO_2RR generally involves a multiple proton/electron coupled process, many kinds of products such as CO, CH_4, HCHO, CH_3OH, CH_4, and C_2H_5OH could be produced.[63] In addition, the thermodynamic potentials between different CO_2RR reactions are close and comparable to that of HER. This leads to the fact that H_2 is the major side-product in CO_2RR and that the product of CO_2RR is usually not a single species but mixed products containing several component species, resulting in poor selectivity. As for CO_2RR on M−N_4 (M=Cr, Mn, Fe, Co, Ni), experimental results found that large amounts of H_2 and CO can be produced with a tiny amount of CH_4, and liquid products are rarely detected by ^{1}H Nuclear magnetic resonance (NMR).[26,35,64] The appealing selectivity of CO is because M centers have a weak binding strength with CO intermediate, which makes the adsorbed CO have a higher chance to desorb from catalyst surface instead of being further reduced into hydrocarbons and oxygenates.[26,35,56] As for the HER competition, many studies have demonstrated that metallic species work differently from M−N_X in catalyzing CO_2RR and HER, and it is generally accepted that metallic species prefers to catalyze HER rather than CO_2 reduction.[65,66] Therefore, it is of great importance to avoid the formation of heterogeneous metallic structures in M−N_X-C catalysts to achieve highly selective reduction of CO_2 to CO. In this case, the time-consuming and costly processes for separating products in down-stream applications could

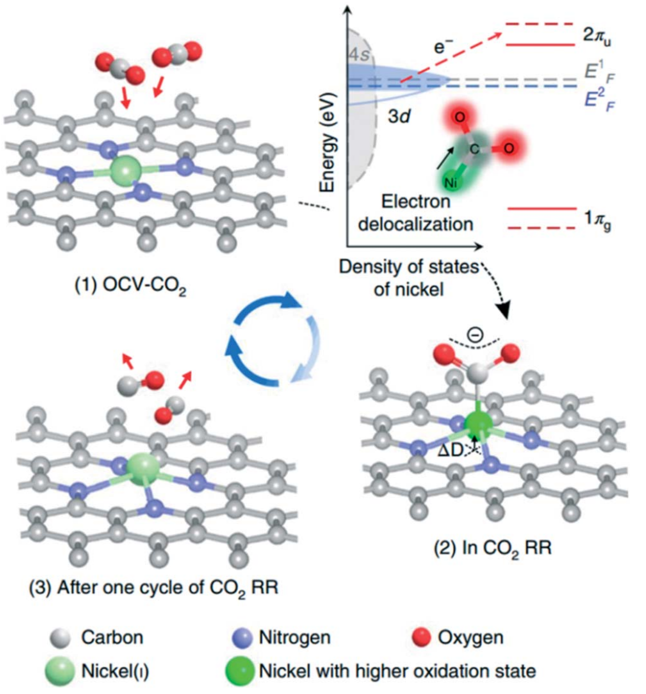

Fig. 2 Structural evolution of the active site in electrochemical CO_2 reduction. e, ΔD in shows the displacement of Ni atom out of plane resulting from electron transfer from Ni atom to CO_2. The upper-right schematic shows the activation processes for CO_2 molecules on the Ni(i) site. A valence band structure, similar to metallic nickel, was used to simplify the schematic illustration. Reproduced with permission from ref. 27 Copyright 2018, Nature.

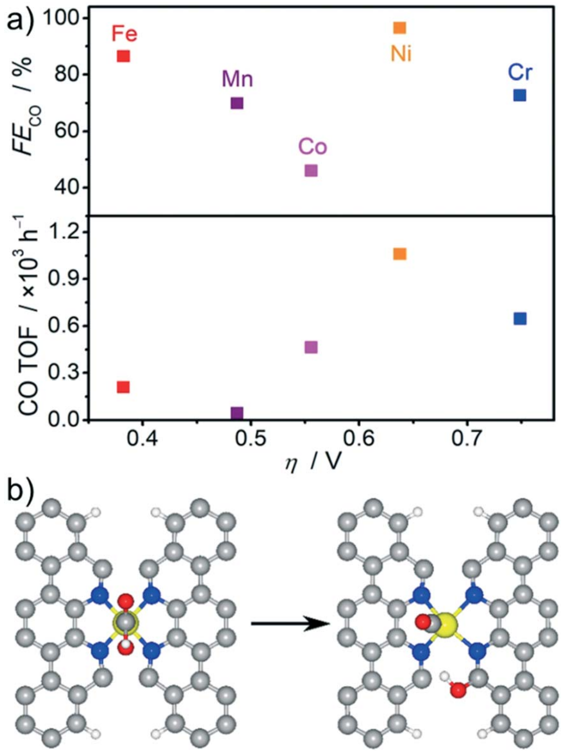

Fig. 3 Summary of maximum CO FEs and TOFs at corresponding overpotentials for transition metal Cr, Mn, Fe, Co, and Ni for CO_2 reduction. Reproduced with permission from ref. 64 Copyright 2017, Elsevier. (b) The initial and final state for the COOH dissociation reaction on $M{-}N_{2+2}$ sites. In the figure, the gray, blue, yellow, red, and white balls represent C, N, M, O, and H atoms, respectively. Reproduced with permission from ref. 56 Copyright 2018, ACS.

be avoided when near-unity CO selectivity can be achieved on $M{-}N_X$-C.

3.3. Design principle

The electrocatalytic performance of a catalyst is mainly determined by the intrinsic activity of each active site (turnover frequency per site, TOF) and the number of effective catalytic sites.[67] Incorporation of the most active species is able to increase the TOF while avoiding the introduction of inactive species with low catalytic property. For this purpose, the electrochemical CO_2RR on a range of transition metals including Cr, Mn, Fe, Co, and Ni have been studied experimentally and theoretically.[35,64] Among these five transition metals, Fe showed the lowest overpotential of 0.38 V to reach a maximum FE of 87% and Ni showed the highest FE of 96% and the highest TOF of 1060 h^{-1} at a moderate overpotential of 0.64 V (Figure 3a).[64] This suggests that Fe and Ni are intrinsically more active than Mn, Co, and Cr. The primary role of Fe was identified to reduce the overpotential, while Ni can significantly improve CO selectivity and boost reaction rates. These findings suggest that using Fe and/or Ni to construct $M{-}N_X$ might be more promising to achieve better performance than using other metals. On the other hand, theoretical identification of active sites has also been conducted. Pan et al.[56] examined the heat of COOH* → CO* + OH*, the rate determining step in CO_2RR, and they established that the breakage of the C−O bond of CO_2 is an exothermic process preferrable on edge-hosted $M{-}N_{2+2}$ containing adjacent carbon atoms with dangling bonds (Figure 3b). In the dissociation of *COOH on $M{-}N_{2+2}$, the M atom is the site for the adsorption of *CO and the N-neighboring carbon atom with dangling bonds is the active center to bond *OH. In contrast, the COOH* dissociation step is an endothermic process requiring more than 1 eV external heat on bulk-hosted $M{-}N_4$ without carbon atoms containing dualing bonds, suggesting that it requires insurmountable activation and making this process impossible. These findings presaged that constructing edge-sosted $M{-}N_{2+2}$ might be more kinetically favorable for CO_2 reduction, providing a possible way to enhance the TOF per M sites by creating more defects (e.g., carbon with dangling bonds) in carbon supports.

The number of effective catalytic sites is highly dependent on dopant concentrations and carbon micro/mesostructure. Dodele and coworkers[49] did a comprehensive investigation on the factors required for the formation of $M{-}N_4$ structure, and the identified four factors are: (i) disordered carbon content, (ii) iron, (iii) surface nitrogen, and (iv) micropores in the catalyst. The disordered phase of carbons can react faster with N-containing sources (eg., NH_3) than the graphitic phase, thus helping fix more nitrogen atoms in the carbon lattice to further bond with the M center. The micropores of the catalysts play a key role in determining the number of active $M{-}N_X$ sites because the micropores host M atoms to further interact with N atoms on the edges of carbon, which also affords more locations to increase the sites for the dopants introduction. Furthermore, the effective active sites are those directly in contact with CO_2, protons, and electrons. Thus, exposing $M{-}N_4$ site, increasing electron mobility and mass transportation are also imperative and can be achieved by improving graphitization degree, increasing surface area, and constructing porous architecture.[14,68] Both inherent properties of $M-N_4$ functionalities and carbon structure need to be considered simultaneously to enhance the overall performance of $M-N_X$-C.

As to the parameters used for activity evaluation, comprehensive consideration of Faradaic efficiency (FE), partial current density (or TOF), and overpotentials should be performed to reflect the energy input, fuel production rate, and selectivity. Since it is highly desirable that CO_2 reduction could maintain high product selectivity and reaction rates with a small energy input, realizing high FE and partial current at a low overpotential is highly desirable in the CO_2 reduction process.

4. Atomic $M-N_X$-C catalysts for CO_2RR

Traditional $M-N_X$-C catalysts were commonly synthesized by pyrolyzing a composite of physically mixed M salts and N/C-containing precursors. Due to high mobility and diffusivity of M atoms, isolated $M-N_X$ will undergo uncontrolled sintering during the high-temperature treatment process, eventually leading to the formation of mixed phases of $M-N_X$ and M-based crystallographic structures in final catalysts. In this case, the atomic utilization efficiency of M centers will be diminished, and the local environments of active sites cannot be well controlled by using traditional synthetic methods. Very recently, many novel strategies on the synthesis of atomically dispersed metal-free $M-N_X$ have been developed, which endow $M-N_X$-C with excellent activity and stability in CO_2RR. In this section, we presented these advances, and the relationships between their CO_2RR activity, structure, and compositions are also discussed.

4.1. $Fe-N_4$-C

Towards the goal of synthesizing well-dispersed atomic Fe site catalysts, Zhang et al.[57] developed an effective thermal activation of chemically Fe-doped zeolitic imidazolate frameworks (Fe-ZIF) approach. Figure 4a depicts the basic synthetic principle for atomic Fe atoms dispersed Fe-N-C catalyst. ZIF-8, composed of zinc bridging with 2-methylimidazole, was employed as the parent MOF in the synthesis since it is rich in N and pores. Fe-ZIF precursors were synthesized by replacing Zn^{2+} with Fe^{3+} during the one-pot synthesis

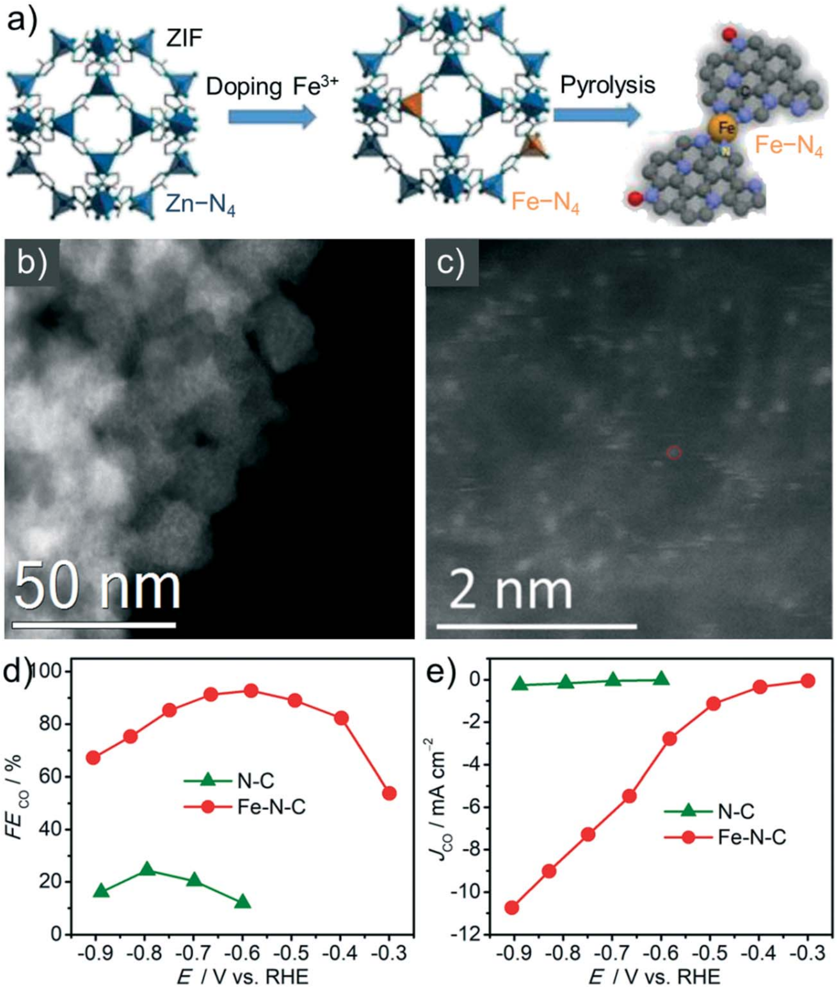

Fig. 4 (a) Synthesis principles of atomic Fe-N-C by pyrolyzing Fe-doped ZIF. Reproduced with permission from ref. 57 Copyright 2017, ACS. (b, c) HAADF-STEM images of Fe-doped ZIF-derived Fe-N-C catalysts. (d) CO FEs and partial current densities of Fe-free N-C and $Fe-N_4$-C catalysts. Reproduced with permission from ref. 56 Copyright 2018, ACS.

of parent ZIF-8, which showed the same crystal structure and rhombic dodecahedron shapes of Fe-free ZIF-8. Rather than physically absorbed in the pores of ZIF-8, Fe ions are nodes that chemically bond with 2-methylimidazole, thus stabilizing atomic Fe dispersion in precursors through covalence bonds. After high-temperature chemical activation at 1100 °C, the atomically dispersed $\mathrm{Fe{-}N_4}$ was obtained. In the heating process, Zn plays two important roles, one being spacers to disperse Fe to avoid the formation of metallic clusters, and the other being pore-forming agents to generate porous carbon structure because of its relatively low boiling point (907 °C).

By characterizing atomic structure of Fe using HAADF-STEM, the isolated and well-dispersed Fe sites were directly observed (Figure 4b-c), both of which were located at edge sites and embedded in the carbon matrix. X-ray absorption spectra also confirmed that Fe atoms were coordinated with four N in the form of $\mathrm{Fe{-}N_4}$ complexes. The ZIF-derived Fe-N-C exhibited an onset potential of −0.29 V for CO_2 reduction in a $KHCO_3$ solution, which was more much positive than that of Fe-free N-doped carbon (−0.67 V) prepared by annealing ZIF-8. Gaseous CO and H_2 were detected as main products with trace amounts of CH_4 (Figure 4d). The Fe-N-C also delivered a maximum CO FE of 93% and CO partial current density of 2.8 mA cm^{-2} at a low overpotential of 470 mV (Figure 4e), significantly higher than those of N-C, suggesting that $\mathrm{Fe{-}N_4}$ is more active in suppressing HER compared to $\mathrm{C{-}N_X}$ sites. The atomic $\mathrm{Fe{-}N_4}$ site was also found to possess excellent electrochemical stability without any decay in CO selectivity and current, and 20 hour reaction yielded a total CO production of 1.0 mmol cm^{-2} at a low overpotential of 470 mV.

The amounts of M ions in the precursors commonly play a key role in the evolution of atomic M sites, and one can assume that there is no way to exclusively synthesize atomic M sites if excessive M ions are introduced. Based on this assumption, Huan et al.[62,65] prepared a set of Fe-based catalysts by annealing a mixture consisting of ZIF-8, ferrous acetate, and phenanthroline (Figure 5a). By accurately adjusting Fe content in precursors, the variable proportion of single-Fe-atom centers and Fe-containing nanoparticles can be controlled. As shown in the Mössbauer spectroscopy (Figure 5b-c), $Fe_{0.5}d$, prepared with lower Fe content, showed the presence of atomically dispersed Fe ions in the N-doped carbon matrix, namely square-planar $\mathrm{Fe^{II}N_4}$ or $\mathrm{Fe^{III}N_4}$ species in low- and medium-spin states (doublets D1 and D2), respectively. Notably, when increasing Fe content in precursors to yield $Fe_{4.0}d$, the formation of Fe crystalline structures was clearly demonstrated, mainly containing iron carbide without discernible amounts of isolated $\mathrm{Fe{-}N_4}$ species. By further exploring structure−selectivity relationship for CO_2 reduction, they have identified that $\mathrm{Fe{-}N_4}$ moieties are the key active sites for the selective CO_2 reduction into CO under aqueous conditions, while Fe nanoparticles mainly catalyze hydrogen evolution. The $Fe_{0.5}d$ exhibited a high and stable Faradaic yield for CO formation of 91% at an overpotential of 490 mV. The CO/H_2 product ratio can also be easily controlled by tuning the ratio of $\mathrm{Fe{-}N_4}$ moieties to iron nanoparticles (Figure 5d), which provides an important route to produce syngas with a tunable CO/H_2 ratio suitable for downstream Fischer−Tropsch synthesis of liquid fuels.

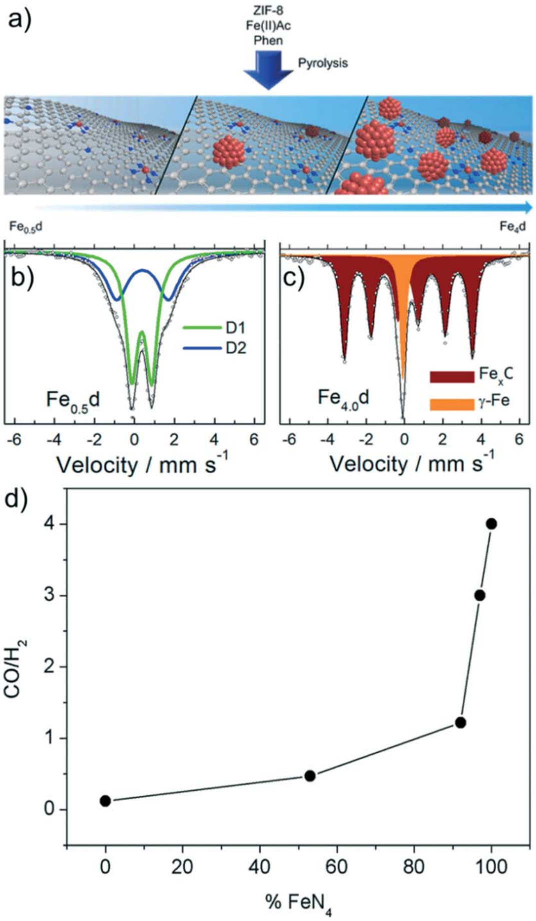

Fig. 5 (a) Schematic representation of the various Fe-N-C materials obtained upon pyrolysis. The amount of Fe nanoparticles increases with increased Fe loading. Fe atoms are represented in red, C atoms in gray, and N atoms in blue. ^{57}Fe Mössbauer absorption spectra of $Fe_{0.5}d$ (b) and Fe_4d (c). (d) CO/H_2 ratio of the gas blend as a function of the relative content of $\mathrm{Fe{-}N_4}$ sites over the total iron content in the materials. Reproduced with permission from ref. 65 Copyright 2017, ACS.

4.2. $\mathrm{Ni{-}N_4}$-C

Ni is another transition metal that has been demonstrated to have enhanced activity for CO_2 reduction. Zhao et al.[66] developed an ionic exchange and ZIF-assisted strategy to generate Ni single atoms distributed in nitrogen-doped porous carbon (Ni SAs/N-C) for active CO_2 reduction. In specific, the initial ZIF-8 was homogeneously dispersed in n-hexane, followed by the injection of $Ni(NO_3)_2$ aqueous solution. Through a double-solvent approach, the Ni precursor could be confined within the pores of ZIF-8, and the mixture was pyrolyzed at 1000 °C under Ar flow. In the heating process, the organic linkers were transformed into N-doped carbon skeleton, and the Zn nodes will evaporate at such high temperatures, which would be easily occupied by the neighboring Ni^{2+} ions, providing a protective fence to avoid Ni aggregation. Hence, the isolated Ni^{2+} ions could be stabilized by N coordination and further reduced by the surrounding carbon. The as-prepared Ni SAs/N-C structure retained the initial rhombododecahedral shape and the Ni atoms dominantly presented the atomic dispersion with a homogeneous distribution. Further XAS characterization proposed that the local Ni structure involved coordination by three N atoms. This single-atom Ni catalyst exhibited a TOF of 5273 h^{-1}, a FE over 71.9%, and a partial current density of 5.5 mA cm^{-2} for CO production at an overpotential of 890 mV.

Although the above ZIF-derived Ni SAs/N-C has the atomic dispersion of Ni atoms, the overall activity is not very notable, probably because the post ionic exchange method could not incorporate adequate Ni atoms and the Ni−N_3 center is not intrinsically efficient for CO_2 activation. Very recently, Li et al.[26] reported a topochemical transformation strategy to prepare exclusive Ni−N_4 catalyst (Ni-N_4-C), which generated the unprecedentedly high activity and selectivity for CO_2 reduction. As shown in Figure 6a, the Ni-doped C_3N_4 prepared from heating freeze-dried powder of dicyandiamide, NH_4Cl and $NiCl_2$ was first coated by a carbon layer, which was achieved by hydrothermal treatment of Ni-doped C_3N_4 in glucose solution. The subsequent high-temperature carbonization generated the Ni−N_4 sites that were inserted in the carbon frameworks. The core of this method is that the carbon layer coating successfully ensures the preservation of the Ni−N_4 structure to a maximized extent and avoids agglomeration of Ni atoms to particles, thus providing abundant active sites. Benefiting from high-density Ni−N_4 sites (Figure 6b), the Ni−N_4-C catalyst showed significantly suppressed H_2 evolution, giving a maximum CO FE of 99% at −0.81 V with a current density of 28.6 mA cm^{-2} (Figure 6c). In contrast, in spite of the existence of Ni, the sample prepared by directly pyrolyzing Ni-doped g-C_3N_4 (Ni@N-C) and the sample made by a pyrolyzing homogeneous mixture of glucose and precursor for Ni-doped g-C_3N_4 (Ni@N-C-Glu) showed poor activity similar to that of Ni-free N−C. These comparisons further unveiled the superiority of atomic Ni−N_4 sites in catalyzing CO_2 reduction.

Li et al. further performed DFT calculation to explore the underlying reason of the high CO selectivity on Ni−N_4.[26] The free energy diagrams of CO_2 reduction for Ni−N_4-C and N−C are presented in Figure 6d, from which the formation of adsorbed intermediate COOH* was found as the potential limiting step. Obviously, the introduction of Ni−N_4 sites lowers the formation energy of COOH* compared with that for N−C, thereby facilitating subsequent CO formation and showing higher activity. Because HER is the major competitive reaction that influence CO selectivity, the difference between thermodynamic limiting potentials for CO_2 reduction and H_2 evolution (denoted as UL(CO_2) − UL(H_2)) was employed as a key parameter to reflect the selectivity in CO_2RR. As seen in Figure 6e, Ni−N_4-C shows a significantly more positive value for UL(CO_2) − UL(H_2) than that of N−C, suggesting a higher selectivity for reduction of CO_2 to CO. This result indicated that the Ni−N_4 structure has lowered energy barrier and accelerated charge transfer in the CO_2 reduction, thus resulting in enhanced activity and selectivity for the conversion of CO_2 to CO.

The selection of suitable carbon supports is also considered a key factor to prepare the atomic catalyst because carbon supports can

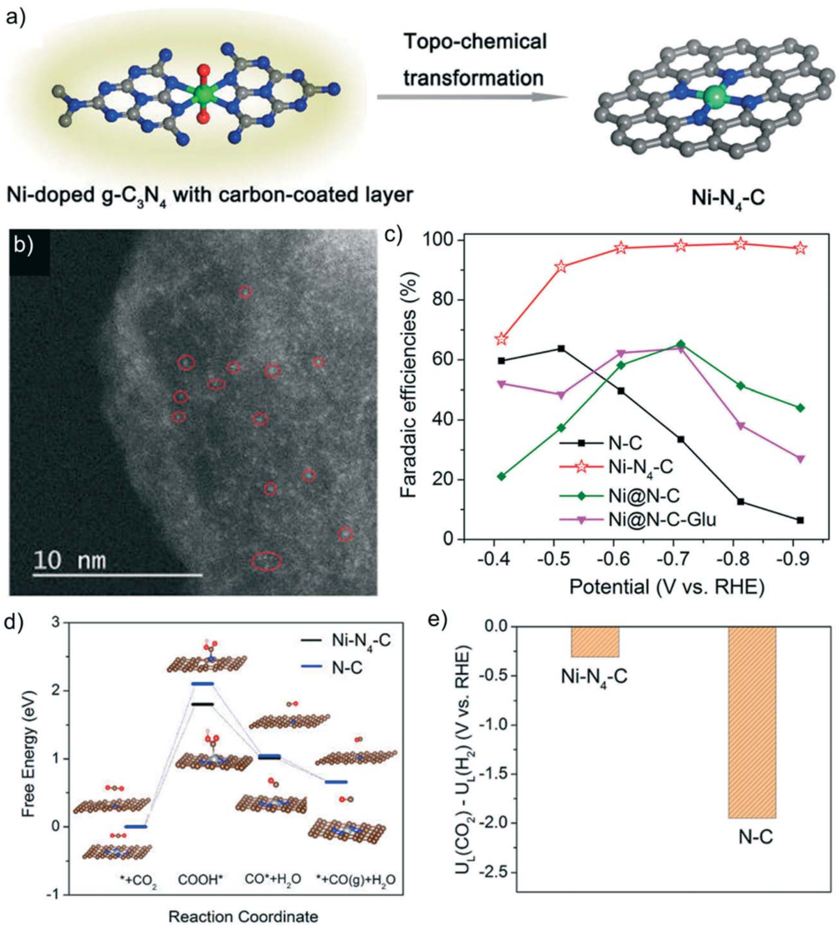

Fig. 6 Schematic illustration of the topo-chemical transformation strategy (Ni atoms, green; N atoms, blue; C atoms, gray; O atoms, red). (b) HAADF-STEM image of Ni−N_4-C. (c) CO FEs of various catalysts. (d) Calculated free energy diagram. (e) Difference in limiting potentials for CO_2 reduction and H_2 evolution. Reproduced with permission from ref. 26 Copyright 2017, ACS.

determine the amounts of absorbed M ions and the location sites for the reaction between M ions and N sources. Jiang et al.[69] developed a graphene oxide (GO)-assisted method to fabricate single M atoms because GO has many merits including high-density defects and negatively-charged surface, which can help adsorb positive M cations. By reducing the amount of Ni adsorbed on GO surface in NH_3 atmosphere, the single-atom Ni catalyst (Ni-NG) was obtained (Figure 7a), which presented a high CO selectivity of 95% and a current of 11 mA cm^{-2} under an overpotential of 550 mV in water with an excellent stability over 20 hours of continuous electrolysis. To further improve current density, an anion membrane electrode assembly was applied using Ni-NG as the cathodic electrode for CO_2RR and IrO_2 as the anodic electrode for oxygen evolution reaction (Figure 7b). This design can help to avoid the direct contact of aqueous electrolyte with CO_2 and facilitate the CO_2 mass transport, thus greatly suppressing the competing HER even under large overpotentials. With the assistance of this configuration, a high current of 50 mA cm^{-2} was achieved with a high CO selectivity of 97% (Figure 7c,d). This represents a new direction to achieve high CO_2 conversion by extending the size of the gas diffusion layer, increasing the catalyst loading, and stacking multiple cells.

Besides the above-mentioned methods that construct atomic M sites using a bottom-up method, the removal of metallic phases by acid leaching, a top-down method, was also used to fabricate atomic M catalysts. For example, Yang et al.[27] synthesized single Ni sites supported on N,S-doped graphene (A-Ni-NSG) by pyrolyzing a mixture of l-cysteine, melamine and nickel acetate in argon, followed by HCl and HNO_3 washing and second heating treatment to recover the carbon crystallinity. This catalyst exhibited high intrinsic CO_2 reduction activity, reaching a specific current of 350 A g^{-1} and a TOF of 14,800 h^{-1} at a mild overpotential of 610 mV for CO production with a FE of 97%. The catalyst also maintained 98% of its initial activity after 100 h of continuous reaction at CO current densities as high as 22 mA cm^{-2}. Compared to bottom-up strategies, these post-treatment processes are more complicated, and it is also challenging to completely eliminate metallic nanoparticles because some particles may be encapsulated into carbon nanotubes or wrapped by carbon sheet layers, preventing them from contacting with acid.[51,54]

4.3. Co−N_2-C

Although numerous findings have demonstrated that Co and N-doped carbons commonly showed inferior CO selectivity due to the favorable HER on Co−N_4 sites,[35,64,69,70] a recent study revealed that the Co−N_2 site is very efficient in reducing CO_2 into CO. Wang et al.[36] realized the fine modulation of N coordination numbers by adjusting pyrolysis temperatures in the carbonization of bimetallic Co/Zn ZIF (Figure 8a). The surrounding N numbers of central Co sites decreased from 4 to 2 when increasing the heating temperature from 800 to 1000 °C. After examining the electrocatalytic CO_2 reduction activity, it was found that Co−N_2 reached a CO FE up to 95 % at −0.68 V (Figure 8b); while Co−N_3 could only achieve a maximum FE of 63 % at −0.53 V, and Co−N_4 had a maximum CO FE lower than 5 % at a more negative potential of 0.83 V, which is similar to Co nanoparticle (below 7%). To confirm the role of Co−N_2, the N coordination number in Co−N_2 was regulated back to 4 by NH_3 treatment at 400 °C (Figure 8c), and they found that the NH_3-treated catalyst exhibited a drastic decline in CO specific current density than the initial Co−N_2

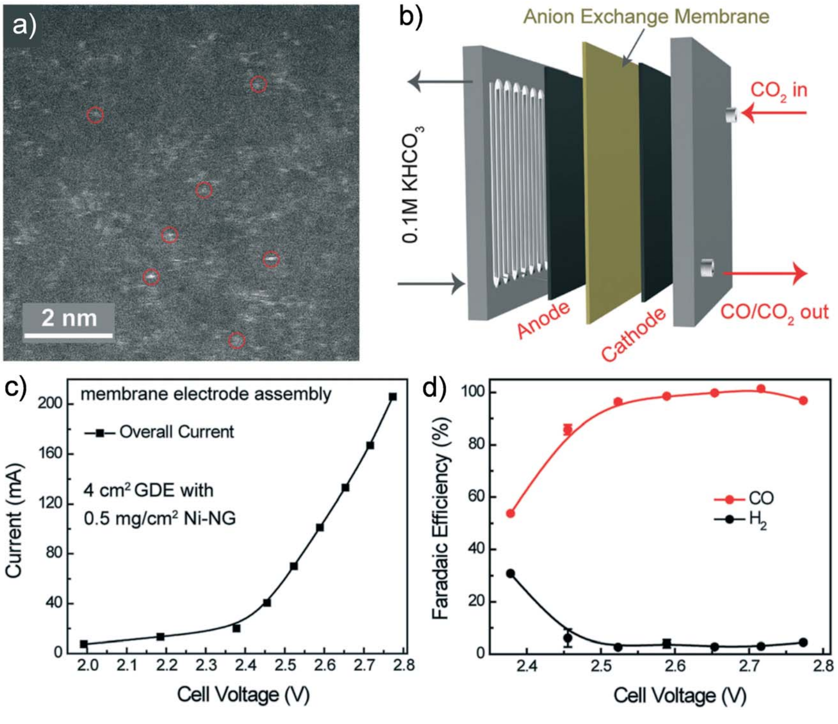

Fig. 7 (a) A HAADF-STEM image of Ni-NG. (b) Schematic of the anion MEA. (c) The steady-state current of Ni-NG (0.5 mg cm^{-2}) on the 4 cm^{-2} electrode and (d) the corresponding FEs of H_2 and CO. Reproduced with permission from ref. 69 Copyright 2018, RSC.

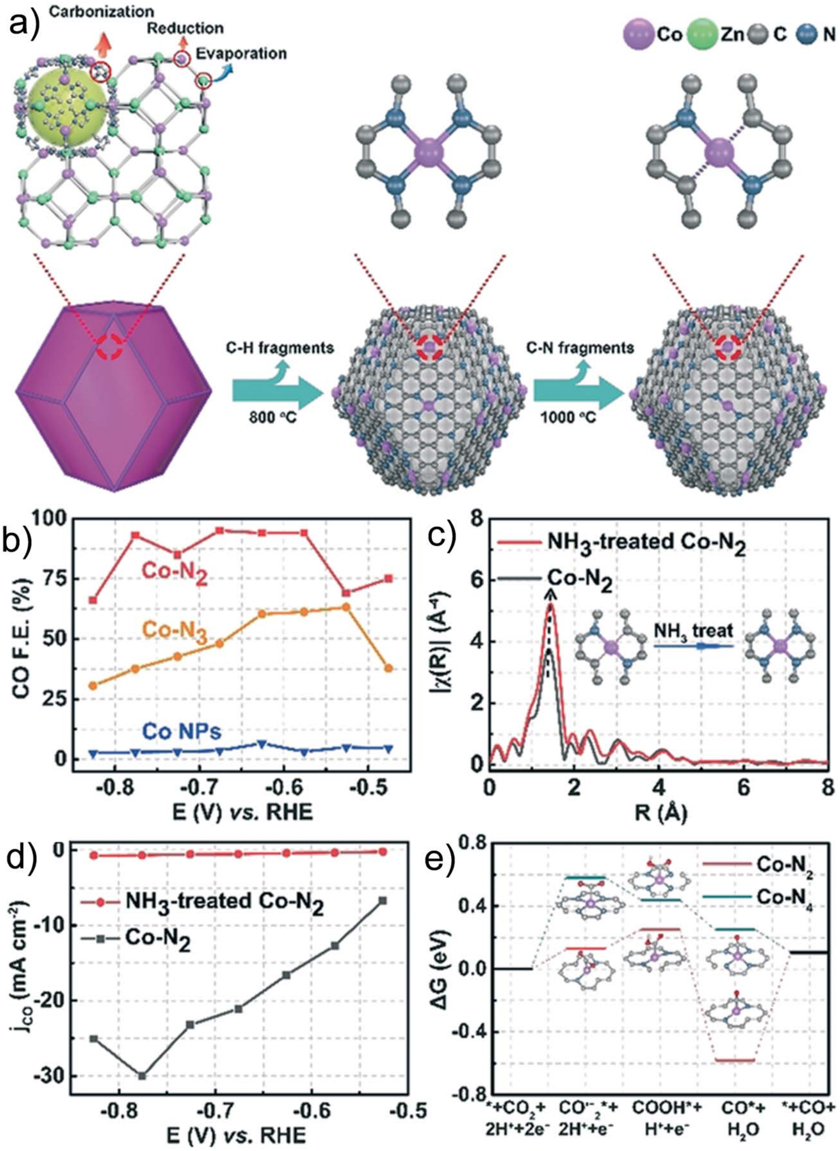

Fig. 8 (a) The formation process of Co−N_4 and Co−N_2. (b) CO FEs at different applied potentials. (c) EXAFS and (d) CO specific current density for Co−N_2 and NH_3-treated Co−N_2. (e) Calculated Gibbs free energy diagrams for CO_2 electroreduction to CO on Co−N_2 and Co−N_4. Reproduced with permission from ref. 36 Copyright 2018, Wiley.

sample (Figure 8d). These results implied that the decreased coordinating N can give rise to a higher CO selectivity and activity. The DFT prediction manifested that both H_2 formation and CO_2 reduction on Co−N_4 are sluggish owing to the high $CO_2^{\cdot-}$* and H* adsorption energy, and the lower energy of H* adsorption compared to $CO_2^{\cdot-}$* adsorption suppresses the CO_2 reduction on Co−N_4. As to Co−N_2, the $CO_2^{\cdot-}$* adsorption energy is low because upward-shifted d-band center generates more unoccupied 3d orbitals of Co atoms in Co−N_2 and hence stronger $CO_2^{\cdot-}$* bonding. As a result, the Co−N_2 gained a CO current of 18.1 mA cm^{-2} at a low overpotential of 520 mV, corresponding to a TOF of 18200 h^{-1}.

4.4. Activity comparison of various M−N_X-C catalysts

To compare the activity level of these recently reported atomic catalysts and their specific advantages, their maximum achievable CO FEs and partial current densities at corresponding overpotentials are summarized in Figure 9. First, it is noteworthy that Fe-based M−N_4-C catalysts showed the lowest overpotential and FEs comparable to Ni- and Co-based catalysts, implying that Fe is advantageous in energy saving to achieve high CO selectivity. Second, it can be found that Ni−N_4-C and Co−N_2-C have a significantly higher CO current than Fe−N_4-C, suggesting that Ni and Co centers might have better capabilities to accelerate the kinetics for CO_2 reduction. Third, M−N_4-C exhibited obvious advantages in terms of lower overpotentials and higher FEs when comparing with state-of-the-art non-precious hexagonal Zn (h-Zn)[71] and cobalt porphyrins-based covalent organic frameworks (Co-COF).[72] This highlights the bright future of developing M−N_4-C for large-scale CO_2 electrolysis. However, compared to noble metals like Ag and Au that possess outstanding activity in CO_2RR,[21,22,73–75] almost all M−N_4-C exhibit higher overpotentials when achieving the same level of CO current or FE. For example, a

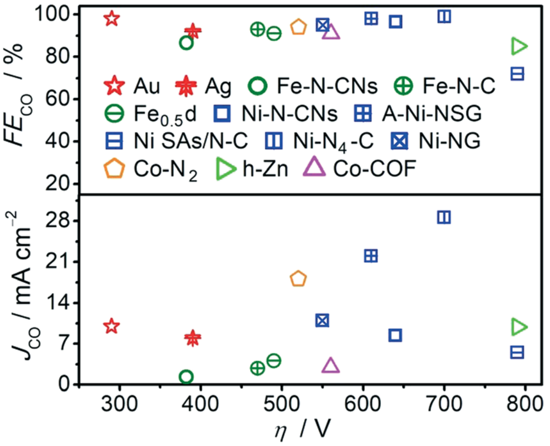

Fig. 9 Comparisons of CO FEs, partial current densities and corresponding overpotentials of M−N$_4$-C with reported non-precious catalysts and noble catalysts. Au;[21] Ag;[22] Fe-N-CNs;[64] Fe-N-C;[56] Fe$_{0.5}$d;[65] Ni-N-CNs;[64] A-Ni-NSG;[27] Ni SAs/N-C;[66] Ni-N$_4$-C;[26] Ni-NG;[69] CO-N$_2$;[36] h-Zn;[71] and Co-COF.[72]

Fe−N$_4$-C catalyst showed comparable CO FE to a porous Ag catalyst at similar overpotentials (87% at 380 mV vs. 92% at 390);[22,64] however, the Fe−N$_4$-C had a much lower CO current compared to the porous Ag (1.3 mA cm^{-2} vs. 8 mA cm^{-2}). Furthermore, when comparing with an oxidized Au catalyst, the Fe−N$_4$-C exhibited a significantly larger overpotential, a lower CO FE, and a smaller CO current (87% and 1.3 mA cm^{-2} at 380 mV for Fe−N$_4$-C vs. 98% and 10 mA cm^{-2} at 290 mV for Au).[21,64] In short, despite accelerating advancements in recent years, there is much room of improvements for M−N$_4$-C electrocatalysts as applicable alternatives to noble metals in practical CO$_2$ electrolysis.

5. Summary and outlook

Electrochemical CO$_2$ reduction has attracted great attention because of the appealing advantages of affording a sustainable way to simultaneously convert greenhouse gas CO$_2$ and store intermittent renewable energy into high-energy-density chemical compounds without regenerating hazardous emissions, making it a promising solution to alleviate the serious changes in ecosystems and modern lives caused by the increasing level of atmospheric CO$_2$. In this review, we present a comprehensive review of recent advances in using atomically dispersed M−N$_X$-C as non-precious electrocatalysts for CO$_2$ reduction, from the aspects of catalytic mechanism, active sites identification, preparation methods, and CO$_2$RR performance. The catalytic properties can be drastically tuned by controlling M atoms, M−N$_X$ configurations, as well as carbon architectures. The striking performance has been achieved on M−N$_X$-C. For instance, a Fe−N$_4$-C catalyst showed an overpotential of 380 mV to reach maximum FE of 87% for CO production, which is comparable to a noble Ag catalyst, and a Fe−N$_4$-C catalyst derived a maximum CO FE of 99% and a current density of 28.6 mA cm^{-2} at an overpotential of 700 mV. Combined with the merits of high atomic utilization efficiency and low-cost, M−N$_X$-C thus holds great promises in future practical CO$_2$ electrolysis application. However, challenges remain in terms of limited understanding of reaction mechanism on specific active sites, low catalytic performance (relatively large overpotentials and low currents) and lack of feasible approaches to prepare atomic catalysts at a large scale. To this end, we recommend future research be performed in the following directions:

(i) **Exploring reaction mechanism.** Systematic understanding of catalytic mechanisms is of great importance to the rational design of high-performance catalysts. Although DFT calculations have been extensively applied, the catalytic mechanism on specific active sites have not been well established, and there is lack of experimental evidence of the intermediates and chemical states changes of M−N$_X$ sites. The surface-sensitive Fourier-transform infrared spectroscopy (FT-IR) and *in situ/operando* XAS are strongly recommended to be employed to help explore the reaction mechanisms. FT-IR could be able to identify the intermediates on the surface of solid-state catalysts and *in situ* XAS could monitor the changes in oxidation states and chemical coordination of M centers during the real CO$_2$ reduction process. Combining DFT productions with experimental investigations, better understanding of the catalytic pathways and roles of active species in CO$_2$RR can be achieved.

(ii) **Engineering M−N$_X$ sites and carbon supports.** The catalytic CO$_2$RR property of M−N$_X$-C is highly dependent on the nature of M−N$_X$ sites and architectures of carbon supports. The edge-hosted M−N$_{2+2}$ has been theoretically suggested to be more efficient than bulk-hosted M−N$_4$. However, the fine configurations of M−N$_X$ by selectively introducing the most active sites is still a big challenge, posing great limitation in improving performance of M−N$_X$-C. More research is thus demanded to develop reliable approaches of controlling the structure of M−N$_X$. In addition, carbon supports play key roles in governing the available number of M−N$_X$, mass transportation of intermediates, as well as mechanical robustness and electrocatalytic stability of catalysts in harsh electrochemical conditions. Thus, engineering the nanostructure of carbon supports also provides opportunities in controlling the activity, selectivity, and stability. However, the relationships between CO$_2$RR performance and carbon structure (morphology, pore sizes, defects, etc.) remain elusive, which should be extensively investigated in the future.

(iii) **Large-scale fabrication of atomic catalysts and design of advanced reactor systems.** The industrial application of M−N$_X$-C for CO$_2$ reduction will not be realistic until large-scale fabrication of atomic catalysts and advanced reactors for the realization of high CO$_2$ conversion rates can be achieved. Present synthesis of atomic M−N$_X$-C is at laboratory-scale, and it is challenging to maintain the high quality of atomic structure while keeping the fabrication cost low in a massive synthesis process. Furthermore, most of current studies have been conducted in a two-chamber cell in aqueous solutions, in which the powder M−N$_X$-C catalysts are loaded on the surface of a current collector. This testing configuration often results in low current density owing to low solubility of CO$_2$ in water. Thereby, designing advanced reactors is necessary for future practical application. Membrane electrode assembly (MEA) may be a good choice, in which the direct contact of CO$_2$ with water can be avoided by separating the anode and cathode with an ion exchange membrane. The anode can be circulated with aqueous electrolyte, and the CO$_2$ can be supplied on the cathode side by gas flow channel. In this case, the mass transportation of CO$_2$ can be largely enhanced by increasing the size of the gas diffusion layer and stacking multiple cells in one system.

Conflicts of interest

There are no conflicts to declare.

Acknowledgments

This work is supported by American Chemical Society – Petroleum Research Fund (ACS-PRF #58167-ND10).

References

1 X. Duan, J. Xu, Z. Wei, J. Ma, S. Guo, S. Wang, H. Liu and S. Dou, *Adv. Mater.*, 2017, **29**, 1701784.
2 D. Pakhare and J. Spivey, *Chem. Soc. Rev.*, 2014, **43**, 7813–7837.
3 J. Artz, T. E. Müller, K. Thenert, J. Kleinekorte, R. Meys, A. Sternberg, A. Bardow and W. Leitner, *Chem. Rev.*, 2018, **118**, 434–504.
4 X. Xiang, H. Zhao, J. Yang, J. Zhao, L. Yan, H. Song and L. Chou, *Appl. Catal. A- Gen.*, 2016, **520**, 140–150.
5 G. A. Olah, G. K. S. Prakash and A. Goeppert, *J. Am. Chem. Soc.*, 2011, **133**, 12881–12898.
6 M. Aresta, A. Dibenedetto and A. Angelini, *Chem. Rev.*, 2014, **114**, 1709–1742.
7 X. Xiang, F. Pan and Y. Li, *Adv. Comp. Hybr. Mater.*, 2018, **1**, 6–31.
8 F. Pan, X. Xiang, W. Deng, H. Zhao, X. Feng and Y. Li, *ChemCatChem*, 2018, **10**, 1–7.
9 L. Liu, C. Zhao, J. Xu and Y. Li, *Appl. Catal. B- Environ.*, 2015, **179**, 489–499.
10 C. Zhao, L. Liu, Q. Zhang, J. Wang and Y. Li, *Catal. Sci. Techno.*, 2012, **2**, 2558–2568.
11 J. Qiao, Y. Liu, F. Hong and J. Zhang, *Chem. Soc. Rev.*, 2014, **43**, 631–675.
12 D. D. Zhu, J. L. Liu and S. Z. Qiao, *Adv. Mater.*, 2016, **28**, 3423–3452.
13 B. A. Rosen, A. Salehi-Khojin, M. R. Thorson, W. Zhu, D. T. Whipple, P. J. A. Kenis and R. I. Masel, *Science*, 2011, **334**, 643–644.
14 C. S. Diercks, Y. Liu, K. E. Cordova and O. M. Yaghi, *Nat. Mater.*, 2018, **17**, 301–307.
15 D. T. Whipple and P. J. A. Kenis, *J. Phys. Chem. Lett.*, 2010, **1**, 3451–3458.
16 B. Kumar, J. P. Brian, V. Atla, S. Kumari, K. A. Bertram, R. T. White and J. M. Spurgeon, *Catal. Today*, 2016, **270**, 19–30.
17 K. P. Kuhl, T. Hatsukade, E. R. Cave, D. N. Abram, J. Kibsgaard and T. F. Jaramillo, *J. Am. Chem. Soc.*, 2014, **136**, 14107–14113.
18 L. Zhang, Z.-J. Zhao and J. Gong, *Angew. Chem. Int. Ed.*, 2017, **56**, 11326–11353.
19 H. Zhao, F. Pan and Y. Li, *J. Materiomics*, 2017, **3**, 17–32.
20 A. Klinkova, P. D. Luna, C.-T. Dinh, O. Voznyy, E. M. Larin, E. Kumacheva and E. H. Sargent, *ACS Catal.*, 2016, **6**, 8115–8120.
21 Y. Chen, C. W. Li and M. W. Kanan, *J. Am. Chem. Soc.*, 2012, **134**, 19969–19972.
22 Q. Lu, J. Rosen, Y. Zhou, G. S. Hutchings, Y. C. Kimmel, J. G. Chen and F. Jiao, *Nat. Commun.*, 2014, **5**, 3242.
23 M. Asadi, K. Kim, C. Liu, A. V. Addepalli, P. Abbasi, P. Yasaei, P. Phillips, A. Behranginia, J. M. Cerrato, R. Haasch, P. Zapol, B. Kumar, R. F. Klie, J. Abiade, L. A. Curtiss and A. Salehi-Khojin, *Science*, 2016, **353**, 467–470.
24 X. Duan, J. Xu, Z. Wei, J. Ma, S. Guo, H. Liu and S. Dou, *Small Methods*, 2017, **1**, 1700156.
25 Y. Liu, Y. Zhang, K. Cheng, X. Quan, X. Fan, Y. Su, S. Chen, H. Zhao, Y. Zhang, H. Yu and M. R. Hoffmann, *Angew. Chem. Int. Ed.*, 2017, **56**, 15607–15611.
26 X. Li, W. Bi, M. Chen, Y. Sun, H. Ju, W. Yan, J. Zhu, X. Wu, W. Chu, C. Wu and Y. Xie, *J. Am. Chem. Soc.*, 2017, **139**, 14889–14892.
27 H. B. Yang, S.-F. Hung, S. Liu, K. Yuan, S. Miao, L. Zhang, X. Huang, H.-Y. Wang, W. Cai, R. Chen, J. Gao, X. Yang, W. Chen, Y. Huang, H. M. Chen, C. M. Li, T. Zhang and B. Liu, *Nat. Energy*, 2018, **3**, 140–147.
28 F. Pan, H. Zhao, W. Deng, X. Feng and Y. Li, *Electrochim. Acta*, 2018, **273**, 154–161.
29 Y. Zhao, J. Liang, C. Wang, J. Ma and G. G. Wallace, *Adv. Energy Mater.*, 2018, **8**, 1702524.
30 Q. Lu and F. Jiao, *Nano Energy*, 2016, **29**, 439–456.
31 D. S. Su, S. Perathoner and G. Centi, *Chem. Rev.*, 2013, **133**, 5782–5816.
32 F. Pan, Z. Cao, Q. Zhao, H. Liang and J. Zhang, *J. Power Sources*, 2014, **272**, 8–15.
33 F. Pan, Y. Duan, X. Zhang and J. Zhang, *ChemCatChem*, 2016, **8**, 163–170.
34 X.-F. Yang, A. Wang, B. Qiao, J. Li, J. Liu and T. Zhang, *Accounts Chem. Res.*, 2013, **46**, 1740–1748.
35 W. Ju, A. Bagger, G.-P. Hao, A. S. Varela, I. Sinev, V. Bon, B. Roldan Cuenya, S. Kaskel, J. Rossmeisl and P. Strasser, *Nat. Commun.*, 2017, **8**, 944.
36 X. Wang, Z. Chen, X. Zhao, T. Yao, W. Chen, R. You, C. Zhao, G. Wu, J. Wang, W. Huang, J. Yang, X. Hong, S. Wei, Y. Wu and Y. Li, *Angew. Chem. Int. Ed.*, 2018, **57**, 1944–1948.
37 J. Masa, W. Xia, M. Muhler and W. Schuhmann, *Angew. Chem. Int. Ed.*, 2015, **54**, 10102–10120.
38 F. Pan, J. Jin, X. Fu, Q. Liu and J. Zhang, *ACS Appl. Mater. Inter.*, 2013, **5**, 11108–11114.
39 D. Guo, R. Shibuya, C. Akiba, S. Saji, T. Kondo and J. Nakamura, *Science*, 2016, **351**, 361–365.
40 F. Pan, Y. Duan, A. Liang, J. Zhang and Y. Li, *Electrochim. Acta*, 2017, **238**, 375–383.
41 Z.-H. Sheng, L. Shao, J.-J. Chen, W.-J. Bao, F.-B. Wang and X.-H. Xia, *ACS Nano*, 2011, **5**, 4350–4358.
42 F. Pan, S. Guo and J. Zhang, *Electrochim. Acta*, 2015, **180**, 29–36.
43 J. Jin, F. Pan, L. Jiang, X. Fu, A. Liang, Z. Wei, J. Zhang and G. Sun, *ACS Nano*, 2014, **8**, 3313–3321.
44 L. Lin, Q. Zhu and A.-W. Xu, *J. Am. Chem. Soc.*, 2014, **136**, 11027–11033.
45 M. Salavati-Niasari and A. Amiri, *Appl. Catal. A- Gen.*, 2005, **290**, 46–53.
46 X. Cui, S. Yang, X. Yan, J. Leng, S. Shuang, P. M. Ajayan and Z. Zhang, *Adv. Funct. Mater.*, 2016, **26**, 5708–5717.
47 U. I. Kramm, I. Herrmann-Geppert, J. Behrends, K. Lips, S. Fiechter and P. Bogdanoff, *J. Am. Chem. Soc.*, 2016, **138**, 635–640.

48 A. Zitolo, N. Ranjbar-Sahraie, T. Mineva, J. Li, Q. Jia, S. Stamatin, G. F. Harrington, S. M. Lyth, P. Krtil, S. Mukerjee, E. Fonda and F. Jaouen, *Nat.Commun.*, 2017, **8**, 957.

49 M. Lefèvre, E. Proietti, F. Jaouen and J. P. Dodelet, *Science*, 2009, **324**, 71–74.

50 F. Pan, Q. Zhao, J. Wang and J. Zhang, *ChemElectroChem*, 2015, **2**, 2032–2040.

51 G. Wu, K. L. More, C. M. Johnston and P. Zelenay, *Science*, 2011, **332**, 443.

52 Q. Zhao, Q. Ma, F. Pan, J. Guo and J. Zhang, *Ionics*, 2016, **22**, 2203–2212.

53 Q. Liu, C. Chen, F. Pan and J. Zhang, *Electrochim. Acta*, 2015, **170**, 234–241.

54 H. T. Chung, D. A. Cullen, D. Higgins, B. T. Sneed, E. F. Holby, K. L. More and P. Zelenay, *Science*, 2017, **357**, 479–484.

55 H. Fei, J. Dong, Y. Feng, C. S. Allen, C. Wan, B. Volosskiy, M. Li, Z. Zhao, Y. Wang, H. Sun, P. An, W. Chen, Z. Guo, C. Lee, D. Chen, I. Shakir, M. Liu, T. Hu, Y. Li, A. I. Kirkland, X. Duan and Y. Huang, *Nat. Catal.*, 2018, **1**, 63–72.

56 F. Pan, H. Zhang, K. Liu, D. A. Cullen, K. L. More, M. Wang, Z. Feng, G. Wang, G. Wu and Y. Li, *ACS Catal.*, 2018, **8**, 3116–3122.

57 H. Zhang, S. Hwang, M. Wang, Z. Feng, S. Karakalos, L. Luo, Z. Qiao, X. Xie, C. Wang, D. Su, Y. Shao and G. Wu, *J. Am. Chem. Soc.*, 2017, **139**, 14143–14149.

58 U. I. Koslowski, I. Abs-Wurmbach, S. Fiechter and P. Bogdanoff, *J. Phys. Chem. C*, 2008, **112**, 15356–15366.

59 U. I. Kramm, J. Herranz, N. Larouche, T. M. Arruda, M. Lefevre, F. Jaouen, P. Bogdanoff, S. Fiechter, I. Abs-Wurmbach, S. Mukerjee and J.-P. Dodelet, *Phys. Chem. Chem. Phys.*, 2012, **14**, 11673–11688.

60 F. Charreteur, F. Jaouen, S. Ruggeri and J.-P. Dodelet, *Electrochim. Acta*, 2008, **53**, 2925–2938.

61 W. Liu, L. Zhang, X. Liu, X. Liu, X. Yang, S. Miao, W. Wang, A. Wang and T. Zhang, *J. Am. Chem. Soc.*, 2017, **139**, 10790–10798.

62 A. Zitolo, V. Goellner, V. Armel, M.-T. Sougrati, T. Mineva, L. Stievano, E. Fonda and F. Jaouen, *Nat. Mater.*, 2015, **14**, 937–942.

63 K. P. Kuhl, E. R. Cave, D. N. Abram and T. F. Jaramillo, *Energ. Environ. Sci.*, 2012, **5**, 7050–7059.

64 F. Pan, W. Deng, C. Justiniano and Y. Li, *Appl. Catal. B-Environ*, 2018, **226**, 463–472.

65 T. N. Huan, N. Ranjbar, G. Rousse, M. Sougrati, A. Zitolo, V. Mougel, F. Jaouen and M. Fontecave, *ACS Catal.*, 2017, **7**, 1520–1525.

66 C. Zhao, X. Dai, T. Yao, W. Chen, X. Wang, J. Wang, J. Yang, S. Wei, Y. Wu and Y. Li, *J. Am. Chem. Soc.*, 2017, **139**, 8078–8081.

67 Z. W. Seh, J. Kibsgaard, C. F. Dickens, I. Chorkendorff, J. K. Nørskov and T. F. Jaramillo, *Science*, 2017, **355**, 1–12.

68 F. Pan, A. Liang, Y. Duan, Q. Liu, J. Zhang and Y. Li, *J. Mater. Chem. A*, 2017, **5**, 13104–13111.

69 K. Jiang, S. Siahrostami, T. Zheng, Y. Hu, S. Hwang, E. Stavitski, Y. Peng, J. Dynes, M. Gangisetty, D. Su, K. Attenkofer and H. Wang, *Energ. Environ. Sci.*, 2018, **11**, 893–903.

70 H. Fei, J. Dong, M. J. Arellano-Jimenez, G. Ye, N. Dong Kim, E. L. G. Samuel, Z. Peng, Z. Zhu, F. Qin, J. Bao, M. J. Yacaman, P. M. Ajayan, D. Chen and J. M. Tour, *Nat. Commun.*, 2015, **6**, 8668.

71 D. H. Won, H. Shin, J. Koh, J. Chung, H. S. Lee, H. Kim and S. I. Woo, *Angew. Chem. Int. Ed.*, 2016, **55**, 9297–9300.

72 S. Lin, C. S. Diercks, Y.-B. Zhang, N. Kornienko, E. M. Nichols, Y. Zhao, A. R. Paris, D. Kim, P. Yang, O. M. Yaghi and C. J. Chang, *Science*, 2015, **349**, 1208–1213.

73 D. Gao, H. Zhou, J. Wang, S. Miao, F. Yang, G. Wang, J. Wang and X. Bao, *J. Am. Chem. Soc.*, 2015, **137**, 4288–4291.

74 M. Ma, B. J. Trześniewski, J. Xie and W. A. Smith, *Angew. Chem. Int. Ed. Engl.*, 2016, **55**, 9748–9752.

75 Y. Yoon, A. S. Hall and Y. Surendranath, *Angew. Chem. Int. Ed.*, 2016, **55**, 15282–15286.